Title

Deterministic reversal of single magnetic vortex circulation by an electric field

Journal

Science Bulletin, 65(15)

ISSN

2095-9273

Authors

Zhang, Yuelin

Wang, Chuanshou

Huang, Houbing

et al.

Publication Date

2020-08-01

DOI

10.1016/j.scib.2020.04.008

Peer reviewed

Deterministic reversal of single magnetic vortex circulation by an electric field

Yuelin Zhang[1, #], Chuanshou Wang[1, #], Houbing Huang[2, *], Jingdi Lu[1], Renrong Liang[3], Jian Liu[4], Renci Peng[5], Qintong Zhang[6], Qinghua Zhang[7], Jing Wang[1], Lin Gu[7], Xiu-Feng Han[6], Long-Qing Chen[5, 8], Ramamoorthy Ramesh[4], Ce-Wen Nan[5, *], and Jinxing Zhang[1, *]

[1]Department of Physics, Beijing Normal University, Beijing 100875, P. R. China
E-mail:

[2]Advanced Research Institute of Multidisciplinary Science, Beijing Institute of Technology, Beijing 100081, China

[3]Tsinghua National Laboratory for Information Science and Technology, Institute of Microelectronics, Tsinghua University, Beijing 100084, China

[4]Department of Materials Science and Engineering and Department of Physics, University of California, Berkeley and Materials Science Division, Lawrence Berkeley National Laboratory, Berkeley, CA 94720, USA

[5]State Key Lab of New Ceramics and Fine Processing, School of Materials Science and Engineering, Tsinghua University, Beijing 100084, China
Email:

[6]Beijing National Laboratory of Condensed Matter Physics, Institute of Physics, Chinese Academy of Science, Beijing 100190, China

[7]Beijing National Laboratory of Condensed Matter Physics, Institute of Physics, Chinese Academy of Science, Beijing 100190, China

[8]Department of Materials Science and Engineering, The Pennsylvania State University, University Park, Pennsylvania 16802, USA

[#]These authors contributed equally in this work

[*]Email: hbhuang@bit.edu.cn, cwnan@tsinghua.edu.cn, jxzhang@bnu.edu.cn

Abstract: The ability to control magnetic vortex is critical for their potential applications in spintronic devices. Traditional methods including magnetic field, spin-polarized current etc. have been used to flip the core and/or reverse circulation of vortex. However, it is challenging for deterministic electric-field control of the single magnetic vortex textures with time-reversal broken symmetry and no planar magnetic anisotropy. Here it is reported that a deterministic reversal of single magnetic vortex circulation can be driven back and forth by a space-varying strain in multiferroic heterostructures, which is controlled by using a bi-axial pulsed electric field. Phase-field simulation reveals the mechanism of the emerging magnetoelastic energy with the space variation and visualizes the reversal pathway of the vortex. This deterministic electric-field control of the single magnetic vortex textures demonstrates a new approach to integrate the low-dimensional spin texture into the magnetoelectric thin film devices with low energy consumption.

Keywords: deterministic reversal, electric-field control, space-varying strain, single magnetic vortex, multiferroic heterostructures

1. Introduction

Reversible control of low-dimensional spin structures at nanoscale with low energy consumption is highly desirable for future applications of spintronic devices.[1-4] A vortex is a typical and well-known magnetic domain structure in dimensionally confined nanostructures with a symmetry determined by its polarity and circulation.[5-8] In the past decade, controlling the symmetry (the polarity flipping or the circulation reversal) of such a spin texture has attracted broad interest, which makes it a promising candidate for next-generation magnetic

data-storage devices. Previous studies show that magnetic field or resonant spin-polarized current can effectively control the symmetry of the magnetic vortex. Under the above stimuli, the magnetic vortex core undergoes a gyrotropic precession and its polarity can be flipped. [9-11] Using a magnetic field, magnetic vortex circulation can be reversed from clockwise (anticlockwise) state to anticlockwise (clockwise) state in samples with a thickness gradient.[12]

Manipulation of magnetization using electric field would help reduce the *Joule* heating by several orders of magnitude compared to the traditional stimuli such as magnetic field or current.[13-18] It has been found that electric-field-controlled interfacial orbital reconstruction,[19-20] antiferromagnetic/ferromagnetic exchange[21-22] and static mechanical coupling[23-24] can tune the magnetic anisotropy in magnetoelectric heterostructures. However, the magnetic vortex textures have no planar magnetic anisotropy,[25] the homogenous electric-field control of magnetic vortex cannot induce a broken symmetry (vortex circulation reversal) by the above-mentioned approaches. Several reports showed vortex reversal by homogeneous strain effect but it is uncontrollable duo to involved randomness during the ferroelectric domain switching,[26] and deterministic vortex domain wall control by electric field inside onion-state of magnetic ring.[27] So the symmetry of single vortex circulation cannot be easily broken deterministically, but the magnetic domain is significantly sensitive (grows or shrinks) to the static strain.[28-29] Previous studies demonstrate that varying fields[9, 11, 30] are the key factor to trigger the broken vortex symmetry. This gives us a hint that a space-varying strain (dynamic motion) may be effective to reverse the magnetic vortex circulation deterministically. The reversible in-plane ferroelastic switching with a non-volatile strain of approximately 0.4% in layered-perovskite Bi_2WO_6 (BWO) thin films indicate it is potential for magnetoelectronic

applications and appropriately provide a prototype platform to achieve the considerable planar space-varying strain by electric field. [31-32]

In this work, we clearly demonstrate the deterministic reversal of single magnetic vortex circulation in a $Ni_{79}Fe_{21}$ (NiFe) island on top of a BWO thin film. The NiFe thin film, without in-plane magnetic anisotropy, is an applicable material for formation of vortex square by lithography and control by external stimulation[9]. Piezoresponse force microscopy (PFM) and magnetic force microscopy (MFM) studies demonstrate that the ferroelastic domain wall moves gradually under the planar electric field, accompanied by the space-varying strain and further reversal of the magnetic vortex circulation. Phase-field simulation directly visualizes this dynamic reversal process: magnetic vortex center moves from its equilibrium position to the edge of the NiFe island due to the varying strain in BWO layer and disappears, then a new vortex emerges with opposite circulation, substituting the previous one.

2. Results and Discussion

2.1. Fabrication and Characterization of NiFe/BWO heterostructures

Epitaxial BWO thin films (approximately 200 nm thick) have been grown using pulsed laser deposition (PLD) on perovskite $SrTiO_3$ (STO) substrates. NiFe thin films (~20 nm thick) with Au protection layer (~3 nm thick) have been grown by magnetron sputtering on top of BWO thin films. Our high-resolution scanning transmission electron microscope (STEM) image of BWO/STO interface show the good epitaxy of the BWO thin film (Figure S1a, Supporting Information), and θ-2θ X-ray diffraction (XRD) analysis of the NiFe/BWO heterostructures reveals a high-quality single crystalline BWO and polycrystalline NiFe (Figure S1b, Supporting Information). The detailed growth conditions can be found in the

Methods. High-resolution atomic force microscopy (AFM) (Figure S1c, Supporting Information) shows the NiFe thin film highly follows the step-flow morphology of the layered-perovskite BWO thin film. The vibrating sample magnetometer (VSM) measurement indicates that there is no in-plane magnetic anisotropy (Figure S1d, Supporting Information). Energy dispersive X-ray spectroscopy analysis confirms that the chemical composition of the NiFe island (Figure S1e, Supporting Information).

Using electron-beam lithography, NiFe square islands (1×1 μm^2) with a magnetic vortex texture on top of the BWO thin film were fabricated. MFM and X-ray photoemission electron microscopy (PEEM) were used to characterize the magnetic domain and vortex texture of the NiFe islands. Two types of as-grown magnetic vortex domains are shown in **Figure 1**a, b, respectively. MFM phase contrast (bright to dark and dark to bright along the white dashed lines) describes the magnetic stray fields from NiFe islands, which determine the clockwise and anticlockwise circulations of the vortex textures (Figure 1c). The as-grown magnetic vortex was not affected by the tip with a low-moment CoCr coating (stray field ~30 Oe)[5, 33-35] even after multiple scans (Figure S2, Supporting Information). In order to further confirm the vortex circulations, we performed PEEM measurement on the above two NiFe islands on top of BWO thin film which have been already characterized by MFM (left images in Figure 1a, b). A grounded conductive Pt layer was coated overall the sample surface to prevent the surface charging. The PEEM results show the clockwise and anticlockwise magnetic circulations (right images in Figure 1a, b) as defined by MFM. A NiFe island with four planar electrodes was fabricated on top of the BWO thin film (Figure 1d). This magnetoelectric device is used to study the magnetic vortex texture under the application of planar electric field. The detailed

measurements for θ-2θ XRD, AFM, MFM and PEEM are given in the Methods.

2.2. Vortex circulation reversal by electric field

A pulsed electric field (number ~5000, width ~10 μs) was applied using electrodes #1, #2, #3 and #4 of the devices. As shown in Figure S3b, the ferroelectric domain evolution is revealed by in-plane PFM characterization as a function of electric field (50-400 $kVcm^{-1}$) which was applied on BWO thin film using electrodes #1 and #3 (along downward direction). The corresponding magnetic domain (anticlockwise circulation) of the NiFe island was also captured after removal of the electric fields. We observe that the magnetic vortex center started to move off its original equilibrium position during the ferroelectric domain completely switched to mono-domain under an electric field of 400 $kVcm^{-1}$, indicating a direct coupling of magnetic and elastic orders in the NiFe/BWO heterostructure. The detailed application of electric field and PFM measurement can be seen in Methods. A further pulsed electric field of 500 $kVcm^{-1}$ fulfilled an in-plane polarization switching from the as-grown ferroelectric multi-domain to a nearly mono-domain state (**Figure 2**a, b). We observe that the magnetic vortex circulation was still anticlockwise after removal of the electric field, which kept the same circulation as its as-grown state (Figure 2e, f). When an electric field of 500 $kVcm^{-1}$ was applied on BWO thin film using electrodes #2 and #4 (pointing right), where the ferroelectric domain was switched by 90º (Figure 2c), a reversal of magnetic vortex circulation from anticlockwise to clockwise state occurred (Figure 2g). A further electric field of 500 $kVcm^{-1}$ was applied using electrodes #1 and #3 (along downward direction) so that the 90º ferroelastic domain switching occurred again in BWO thin film (Figure 2d), which triggered that the vortex

circulation reversed back from clockwise to anticlockwise state (Figure 2h). The repeatable back-and-forth reversal of vortex circulation on the same structure is demonstrated (Figure S4, Supporting Information). The above control is repeatable and was achieved in multiple devices. In comparison, there is no reversal of magnetic vortex circulation when the bi-axial electric field was applied on NiFe/STO with the same device structure (Figure S5, Supporting Information). The above experimental observation indicates that the ferroelastic strain during 90º switching from BWO thin film under electric field drives the reversal of magnetic vortex circulation.

2.3. Varying strain under the electric field

In order to clarify the detailed mechanism of the above coupling, dynamic ferroelastic switching process of the BWO thin film, pulsed electric field of ~500 $kVcm^{-1}$ was applied on the device without NiFe islands using planar electrodes (**Figure 3**a). Firstly, the application of the electric field using electrodes #1 and #3 (downward direction) creates a ferroelectric mono-domain structure with a downward polarization, and the size of the mono-domain is much larger than that of the vortex island indicated by the white dashed square. Further PFM studies as a function of pulse number of the electric field have been carried out using electrodes #2 and #4. The ferroelectric domain started to switch and a 90º ferroelastic domain wall nucleated close to the electrode #2 when the electric field with one pulse was applied. After 10 pulses are applied, the ferroelastic domain wall moved across the dashed-square area. Eventually the ferroelastic domain wall reached close to electrode #4 when the electric field with 1000 pulses was applied and a ferroelectric mono-domain with a rightward polarization formed. The

ferroelastic domain-wall motion indicates that the polarization switching dynamics induce the space-varying strain. As shown in Figure 3b, the corresponding varying strain can be excluded by

$$\varepsilon_{11}^{P}(\boldsymbol{r},\mathrm{t}) = Q_{11}P_1^2(\boldsymbol{r},\mathrm{t}) + Q_{12}(P_2^2(\boldsymbol{r},\mathrm{t}) + P_3^2(\boldsymbol{r},\mathrm{t})) \quad (1)$$

$$\varepsilon_{22}^{P}(\boldsymbol{r},\mathrm{t}) = Q_{11}P_2^2(\boldsymbol{r},\mathrm{t}) + Q_{12}(P_1^2(\boldsymbol{r},\mathrm{t}) + P_3^2(\boldsymbol{r},\mathrm{t})) \quad (2)$$

where Q_{11} and Q_{12} are electrostrictive coefficients, and $P_1(\boldsymbol{r},\mathrm{t}), P_2(\boldsymbol{r},\mathrm{t}), P_3(\boldsymbol{r},\mathrm{t})$ are three components of polarization. The pulse-dependent ferroelastic domain-wall motion has been also repeated along downward direction (Figure S6, Supporting Information), so the space-varying strain can be induced in both rightward and downward directions, triggering the back-and-forth reversal of vortex circulation deterministically (Figure S4, Supporting Information). The domain-wall motion can be also achieved underneath the NiFe island, which has been revealed by the PFM studies before and after the island was removed (Figure S7, Supporting Information). These results provide the evidence that the deterministic reversal of magnetic vortex circulation is induced by the planar space-varying strain from BWO thin film under the bi-axial electric field.

2.4. Dynamic mechanism of magnetic vortex reversal

To further elucidate the reversal mechanism of the magnetic vortex circulation by electric-field-induced varying strain of BWO layer, phase-field model by solving the time-dependent Ginzburg-Landau (TDGL) equation[36] is employed for the temporal evolution of the polarization vector under pulsed electric field, and the dynamic evolution of magnetic vortex texture in NiFe island is visualized by micromagnetic simulation with phase-field

microelasticity using a Landau-Lifshitz-Gilbert (LLG) equation.[37] As seen in **Figure 4**a, the dynamic reversal of magnetic vortex from anticlockwise to clockwise circulation was obtained, driven by the corresponding space-varying strain (Figure 4,c). A rightward varying strain moved from the left edge of the vortex texture dragged the vortex center to the left edge of the island within 5 us. Furthermore, the varying strain continuously moved rightward in 10 us, leading to the disappearance of the vortex center and an emergence of a new vortex with opposite circulation from the right edge of the island. This new vortex gradually moved to the center when the varying strain reached across the island. The whole reversal process from anticlockwise to clockwise circulation is completed within 15 us. The detailed space-varying strain induced reversal of vortex circulation can be further seen in the Supporting Information Video. To explain the mechanism of the varying-strain-induced the magnetic vortex reversal, we can describe the elastic effective field $\mathbf{H}_{elas}$ as a function of space-varying strain. The elastic effective field can be expressed by

$$H_{elas}^{x} = \frac{2B_2^2 m_x m_z^2}{c_{44}} - 2B_1 \varepsilon_{11}^{p}(\boldsymbol{r}, t) m_x \quad (3)$$

$$H_{elas}^{y} = \frac{2B_2^2 m_y m_z^2}{c_{44}} - 2B_1 \varepsilon_{22}^{p}(\boldsymbol{r}, t) m_y \quad (4)$$

where B_1=-1.5λ_{100}(c_{11}-c_{12}) and B_2=-3$\lambda_{111}c_{44}$, with λ_{100}, λ_{111} and c_{11}, c_{12}, c_{44} representing the magnetostrictive coefficients, and elastic constants, respectively. $\varepsilon_{11}^{p}(\boldsymbol{r}, t)$ and $\varepsilon_{22}^{p}(\boldsymbol{r}, \mathrm{t})$ are space-varying strain and denote the contribution from the piezoelectric transformation of the bottom BWO layer. In comparison, a static strain (up to 0.8%) without motion cannot induce the circulation reversal although the growth and shrink of the magnetic domain are observed (Figure S8, Supporting Information). The detailed phase-field methods for dynamic simulation are given in the Methods.

3. Conclusions

To conclude, in this magnetoelectric device consisted of NiFe islands with magnetic vortex structure on top of BWO thin films, the vortex circulation can be deterministically reversed *via* the space-varying strain driven by the bi-axial electric field. The dynamic coupling of varying strain and the magnetic vortex circulation have been revealed by a combination of scanning probe techniques and phase-field simulation. This reversible electric-field control of the magnetic vortex symmetry demonstrates a new framework to manipulate low-dimension chiral spin textures with low energy consumption. [38-39] It also provides a promising pathway to integrate the coupling of this varying strain with other functionalities in thin film devices.

4. Experimental Section

Heterostructure growth and device fabrication: (001)-orintated BWO thin films were grown on STO substrates using PLD (248 nm excimer). Stoichiometric BWO (5% excess of Bi_2O_3 in order to compensate the volatile Bi at high growth temperature) targets were ablated at a laser energy density of ~1 J cm^{-2} and a repetition rate of 1 Hz for the growth of BWO (thickness up to 200 nm). For the growth of BWO, the substrate temperature was 720 ºC at anoxygen pressure of 100 mtorr. Afterwards, the films were cooled to room temperature at 0.1 atm of oxygen with a cooling rate of 5 ºC min^{-1}. The $Ni_{79}Fe_{21}$ islands (~ 20 nm thick, 1×1 μm^2) with four electrodes were fabricated on BWO/STO and STO by magnetron sputtering assisted by electron beam lithography (JEOL JBX6300FS).

X-ray diffraction: X-ray θ-2θ scans were obtained by high-resolution X-ray diffraction (Lab XRD-6000, SHIMADZU).

AFM、*PFM and MFM*: The AFM measurements were carried out on tapping mode with ultra-sharp Si tips. The PFM measurements were carried out on a Bruker Multimode 8 AFM with commercially available TiPt-coated Si tips (Mikro Masch) with a tip curvature radius of less than 30 nm. The typical tip-scanning velocity was 2 μm s^{-1}. The amplitude and frequency of the AC input were 1.5 V_{pp} and 22 kHz respectively. High-resolution PFM images were acquired on a wide array of samples. The polarization vectors have been re-constructed based on the domain images obtained from the cantilever scanning parallel and perpendicular to the BWO [100] axis, respectively. The magnetic vortex textures were characterized by a tapping-mode MFM using commercially available low-moment Co-Cr-coated Si tips (MESP, Bruker). The magnetization of the tip was magnetized along the same direction before each scanning

using external magnetic field up to 1000 Oe. During the measurements, typical scanning rate of the cantilever was 1 Hz. The distance between tip and sample surface was set to 100 nm on average. Sample scans were taken in air at ambient temperature.

PEEM: PEEM measurements were completed at PEEM 3 at the Lawrence Berkeley National Laboratory, Advanced Light Source. Focused X-rays were incident on the sample at an angle of 30º from the surface and formed a spot of ~ 9 μm diameter on the sample. Before the imaging, a Pt layer has been coated overall the NiFe-BWO sample to prevent the surface charging during the measurement. Imaging was done by tuning the photon energy to the Ni L-edge (780 eV) and the use of right- and left-handed circularly polarized radiation enabled imaging of the $Ni_{79}Fe_{21}$domain structure by exploiting the XMCD effect at the Ni L_3- and L_2-edges.

Application of in-plane pulsed electric field: The pulsed electric fields were controlled using bi-axial electrodes with a Keithely 2410 SourceMeter. The pulsed electric fields were up to 500 $kVcm^{-1}$ with a maximum frequency of 100 kHz.

Phase-field simulation: Ferroelastic polarization switching in Bi_2WO_6 thin films was simulated using the phase-field simulation by solving the time-dependent Ginzburg-Landau (TDGL) equation for the temporal evolution of the polarization vector field,

$$\frac{\partial \boldsymbol{P_i}(\boldsymbol{r},t)}{\partial t} = -L\frac{\delta F}{\delta \boldsymbol{P_i}(\boldsymbol{r},t)}, i = 1,2,3 \quad (5)$$

where $\boldsymbol{P_i}(\boldsymbol{r},t)$ is the polarization, L is a kinetic coefficient that is related to the domain wall mobility, and F is the total free energy that includes contributions from the Landau energy, elastic energy, electric energy, and gradient energy.

$$F = \iiint \left(f_{Landau} + f_{elastic} + f_{electric} + f_{grad}\right) dV \quad (6)$$

Detailed descriptions of the total free energy *F* were presented in some depth in our previous publication [36]. For 001-oriented BWO, only in-plane spontaneous emerges determined by the orthorhombic structure, thus the bulk free energy density can be expressed by a fourth-order Landau potential as following:

$$f_{Landau} = \alpha_1(P_1^2 + P_2^2) + \alpha_{11}(P_1^4 + P_2^4) + \alpha_{12}P_1^2P_2^2 \quad (7)$$

Here the Landau coefficients α_1, α_{11}, and α_{12} are 4.03×10^5 (T-1200) VmC^{-1}, 9.7×10^8 Vm^5C^{-1}, and 1.8×10^9 Vm^5C^{-3}, respectively [40-41]. The elastic energy density is described using the expression,

$$f_{elastic} = C_{ijkl}(\varepsilon_{ij} - \varepsilon_{ij}^0)(\varepsilon_{kl} - \varepsilon_{kl}^0) \quad (8)$$

where C_{ijkl} is the elastic stiffness tensor, ε_{ij} and ε_{ij}^0 are the total local strain, and the spontaneous strain in the thin film, respectively. The expressions for the $f_{electric}$, and f_{grad} are described in the reference[35]. Material constants for BWO used in the simulation including the elastic constants, electrostrictive coefficients, dielectric constants, and gradient coefficients are: c_{11} = 1.22×10^{11} N m^{-2}, c_{12}=0.14×10^{11} N m^{-2}, c_{44}=0.54×10^{11} N m^{-2}, Q_{11}=0.017 $C^{-2}m^4$, Q_{12}=-0.01 $C^{-2}m^4$, Q_{44}=0.058 $C^{-2}m^4$, κ_{11}=κ_{11}=κ_{11}=500, g_{11}=2g_{44}=6.0, g_{12}=0.0 [41-42]. The TDGL equation was solved by a semi-implicit Fourier spectral method using a discreet grid of 256 Δx × 256 Δx × 36 Δz (Δx, and Δz are the number of grid points and equals to 10 nm, and 2 nm in this work) with the periodic boundary conditions along x and y directions in the film plane. A thin film was calculated by applying short-circuit boundary conditions in both film surfaces as described in detail in our previous publications [36, 43].

Introduction of the Micromagnetic simulation: In the micromagnetic simulation, the magnetic domain structure of $Ni_{79}Fe_{21}$ island is described by the spatial distribution of the local

magnetization vectors $\mathbf{M}(\mathbf{r}, t)=M_s\mathbf{m}=M_s(m_x, m_y, m_z)$, where M_s and m_i ($i=x, y, z$) represent the saturation magnetization and the direction cosine, respectively, $\mathbf{r}$ and t are the space and the time. The temporal evolution of the magnetization dynamics and thus the domain structure is governed by using a Landau-Lifshitz- Gilbert (LLG) equation, [44-45]

$$\frac{\partial \mathbf{M}}{\partial t} = -\gamma' \mathbf{M} \times \mathbf{H}_{eff} - \frac{\alpha \gamma'}{M_s} \mathbf{M} \times (\mathbf{M} \times \mathbf{H}_{eff}) \tag{9}$$

where $\mathbf{H}_{eff}$ is the effective field, $\gamma'=\gamma/(1+\alpha^2)$, γ is the electron gyromagnetic ratio, and α is the dimensionless damping parameter. The effective field $\mathbf{H}_{eff}$ is given as $\mathbf{H}_{eff}=-(1/\mu_0)\ (\delta E_{tot}/\delta \mathbf{M})$, where μ_0 is the vacuum permeability, E_{tot} is the total free energy of $Ni_{79}Fe_{21}$ island and includes the magnetocrystalline anisotropy E_{mc}, magnetostatic E_{ms}, magnetic exchange E_{ex}, elastic energy E_{el} and thermal fluctuations energy E_{th}. Since the polycrystalline $Ni_{79}Fe_{21}$ island was prepared, we ignored the magnetocrystalline anisotropy energy in this model. The magnetostatic energy E_{ms} was calculated by considering the influence of geometric size on the magnetic domain structures. The magnetostatic energy E_d can be written as, [46]

$$E_d = -\frac{1}{2}\mu_0 \int (\mathbf{H}_{\mathrm{d}}^{\mathrm{hetero}} + \mathbf{H}_{\mathrm{d}}^{\mathrm{shape}}) \cdot \mathbf{M} dV \tag{10}$$

where the heterogeneous contribution $\mathbf{H}_{\mathrm{d}}^{\mathrm{hetero}}$ and the demagnetization part $\mathbf{H}_{\mathrm{d}}^{\mathrm{shape}}$ are obtained by solving the magnetostatic equilibrium equation, i.e., $\nabla \cdot \left(\mu_0 \mathbf{H}_{\mathrm{d}}^{\mathrm{hetero}} + \mu_0 M_{\mathrm{s}} \mathbf{M} \right) = 0$ and $\mathbf{H}_{\mathrm{d}}^{\mathrm{shape}} = \mathbf{N}\overline{\mathbf{M}}$, respectively. $\boldsymbol{N}$ is the sample-shape dependent demagnetizing factor matrix and $\overline{\mathbf{M}}$ is the average magnetization field.

The elastic energy E_{elas} was calculated based on a previously developed phase-field model [47] for a three-phase system that is comprised of an isolated magnetic island (the free layer herein), a stiff substrate, and the air. The elastic energy can be expressed by,

$$E_{elas} = \frac{1}{2}\int c_{ijkl} e_{ij} e_{kl} dV = \frac{1}{2}\int c_{ijkl}(\varepsilon_{ij} - \varepsilon_{ij}^{0})(\varepsilon_{kl} - \varepsilon_{kl}^{0}) dV \quad (11)$$

where c_{ijkl} is the elastic stiffness tensor, e_{ij} is the elastic strain, ε_{ij} is the total strain, and ε_{ij}^{0} is the eigenstrain. The Einstein summation convention is employed and *i*, *j*, *k*, l= 1, 2, 3. Based on Khachaturyan's microelastic theory, the total strain ε_{ij} can be divided into homogeneous and heterogeneous strains,

$$\varepsilon_{ij} = \overline{\varepsilon_{ij}} + \eta_{ij} \quad (12)$$

The heterogeneous strain η_{ij} is satisfied by $\int \eta_{ij} dV = 0$. The homogeneous strain $\overline{\varepsilon_{ij}}$ describes the macroscopic shape change of the magnetic island. Specifically, $\overline{\varepsilon_{11}}$ and $\overline{\varepsilon_{22}}$, namely, the homogenous strains along the two in-plane crystal axes, can be expressed as,

$$\begin{aligned} \overline{\varepsilon_{11}} &= \varepsilon_0 + \varepsilon_{11}^{p} \\ \overline{\varepsilon_{22}} &= \varepsilon_0 + \varepsilon_{22}^{p} \end{aligned} \quad (13)$$

where ε_{11}^{p} and ε_{22}^{p} denote the contribution from the piezoelectric transformation of the bottom ferroelastic BWO layer, which we directly use the experimental data reported as the input. In this work, the space-varying strain was adopted as the driving force of magnetization dynamics. The varying strain was described by a diffuse interface shaped function,

$$\begin{aligned} \varepsilon_{11}^{p} &= \varepsilon_{11}^{p_0} \frac{1}{2}[1.0 - \tanh[\frac{x - x_0}{d}]] \\ \varepsilon_{22}^{p} &= \varepsilon_{22}^{p_0} \frac{1}{2}[1.0 - \tanh[\frac{y - y_0}{d}]] \end{aligned} \quad (14)$$

where $\varepsilon_{11}^{p_0}$ and $\varepsilon_{22}^{p_0}$ are the constant strain 0.4% from the experiment, *d* is the a positive parameter. In addition, *x* and *y* are the space coordinate, and x_0 and y_0 is the position increasing with the time. For a polycrystalline magnetic island deposited at the room temperature, we assumed that the biaxial residual strain ε_0 is equal to zero. ε_{ij}^{0} represents the stress-free strain describing the stress-free deformation of a cubic ferromagnetic associated with the local

magnetization change,

$$\varepsilon_{ij}^{0} = \frac{3}{2}\lambda_{100}(m_i m_j - \frac{1}{3}) \quad (i = j) \;\; or \;\; \frac{3}{2}\lambda_{111} m_i m_j \; (i \neq j) \tag{15}$$

where λ_{100} and λ_{111} are the magnetostrictive constants.

The temporal evolution of the local magnetization and thus the domain structures are obtained by numerically solving the LLG equation using the Gauss-Seidel projection method and the semi-implicit Fourier spectral methods with a constant time step Δt= 0.0268858 ps. We adopted the following magnetic parameters, exchange constant A=1.64×10^{-11} J m^{-1}, saturation magnetization M_s=8.78×10^5 A m^{-1}. [48] Other parameters are Gilbert damping parameter α=0.0085, electron gyromagnetic ratio γ=2.40565×10^5 m (A·s) $^{-1}$, elastic constants c_{11}=2.46×10^{11} N m^{-2}, c_{12}=1.47×10^{11} N m^{-2}, c44=0.49×10^{11} N m^{-2}, magnetostrictive constants λ_{100}=λ_{111}=10 ppm. [49]

Supporting Information

1, Supporting Information word of more Figures.

2, Supporting Information Video of dynamic reversal of magnetic vortex

Acknowledgement

Y. Zhang and C. Wang contributed equally to this work. The work in Beijing Normal University is supported by the National Key Research and Development Program of China through Contract No. 2016YFA0302300, National Natural Science Foundation of China (Grant No. 11974052, 51972028) and the support from CAS Interdisciplinary Innovation Team. L.Q.C is supported by the U.S. DOE, Office of Basic Energy Sciences, Division of Materials Sciences and Engineering under Award No. DE-FG02-07ER46417. R.R. is funded by the Director, Office of Science, Office of Basic Energy Sciences, Materials Science and Engineering Department of the US Department of Energy (DOE) in the Quantum Materials Program (KC2202) under Contract No. DE-AC02-05CH11231. J.L. acknowledges the support by the Science Alliance Joint Directed Research & Development Program and the Transdisciplinary Academy Program at the University of Tennessee. Use of the Advanced Light Source is supported by the Director, Office of Science, Office of Basic Energy Sciences, of the US DOE under Contract DE-AC02-05CH11231.

REFERENCES

[1] S. D. Bader, *Reviews of modern physics* **2006**, 78, 1.

[2] S. D. Bader, S. S. P. Parkin, *Annu Rev Conden Ma P* **2010**, 1, 71.

[3] S. Fusil, V. Garcia, A. Barthelemy, M. Bibes, *Annu Rev Mater Res* **2014**, 44, 91.

[4] H. An, H. J. Hong, Y.-R. Jo, S.-G. Jung, S. Kim, S. Kim, J. Lee, H. Choi, H. Yoon, S.-Y. Kim, J. Song, S. Y. Jeong, B. H. Lee, T.-Y. Koo, T. Park, K.-T. Ko, B. Kim, B.-J. Kim, C. W. Bark, S. Lee, *NPG Asia Materials* **2019**, 11, 68.

[5] T. Shinjo, T. Okuno, R. Hassdorf, K. Shigeto, T. Ono, *Science* **2000**, 289, 930.

[6] A. Wachowiak, J. Wiebe, M. Bode, O. Pietzsch, M. Morgenstern, R. Wiesendanger, *Science* **2002**, 298, 577.

[7] S.-B. Choe, Y. Acremann, A. Scholl, A. Bauer, A. Doran, J. Stöhr, H. A. Padmore, *Science* **2004**, 304, 420.

[8] I. A. Malik, H. Huang, Y. Wang, X. Wang, C. Xiao, Y. Sun, R. Ullah, Y. Zhang, J. Wang, M. A. Malik, I. Ahmed, C. Xiong, S. Finizio, M. Kläui, P. Gao, J. Wang, J. Zhang, *Science Bulletin* **2020**, 65, 201.

[9] B. Van Waeyenberge, A. Puzic, H. Stoll, K. Chou, T. Tyliszczak, R. Hertel, M. Fähnle, H. Brückl, K. Rott, G. Reiss, *Nature* **2006**, 444, 461.

[10] K. Yamada, S. Kasai, Y. Nakatani, K. Kobayashi, H. Kohno, A. Thiaville, T. Ono, *Nature materials* **2007**, 6, 270.

[11] A. Vansteenkiste, K. Chou, M. Weigand, M. Curcic, V. Sackmann, H. Stoll, T. Tyliszczak, G. Woltersdorf, C. Back, G. Schütz, *Nature physics* **2009**, 5, 332.

[12] V. Uhlir, M. Urbanek, L. Hladik, J. Spousta, M. Y. Im, P. Fischer, N. Eibagi, J. J. Kan, E. E. Fullerton, T. Sikola, *Nat Nanotechnol* **2013**, 8, 341.

[13] J.-M. Hu, Z. Li, L.-Q. Chen, C.-W. Nan, *Nat Commun* **2011**, 2, 553.

[14] W. Eerenstein, N. Mathur, J. F. Scott, *nature* **2006**, 442, 759.

[15] J. T. Heron, J. L. Bosse, Q. He, Y. Gao, M. Trassin, L. Ye, J. D. Clarkson, C. Wang, J. Liu, S. Salahuddin, D. C. Ralph, D. G. Schlom, J. Iniguez, B. D. Huey, R. Ramesh, *Nature* **2014**, 516, 370.

[16] M. Yang, Y. Deng, Z. Wu, K. Cai, K. W. Edmonds, Y. Li, Y. Sheng, S. Wang, Y. Cui, J. Luo, *Ieee Electr Device L* **2019**, 40, 1554.

[17] K. Cai, M. Yang, H. Ju, S. Wang, Y. Ji, B. Li, K. W. Edmonds, Y. Sheng, B. Zhang, N. Zhang, S. Liu, H. Zheng, K. Wang, *Nat Mater* **2017**, 16, 712.

[18] Y. J. Li, J. J. Wang, J. C. Ye, X. X. Ke, G. Y. Gou, Y. Wei, F. Xue, J. Wang, C. S. Wang, R. C. Peng, X. L. Deng, Y. Yang, X. B. Ren, L. Q. Chen, C. W. Nan, J. X. Zhang, *Advanced Functional Materials* **2015**, 25, 3405.

[19] T. Maruyama, Y. Shiota, T. Nozaki, K. Ohta, N. Toda, M. Mizuguchi, A. A. Tulapurkar, T. Shinjo, M. Shiraishi, S. Mizukami, Y. Ando, Y. Suzuki, *Nature Nanotechnology* **2009**, 4, 158.

[20] V. Garcia, M. Bibes, L. Bocher, S. Valencia, F. Kronast, A. Crassous, X. Moya, S. Enouz-Vedrenne, A. Gloter, D. Imhoff, C. Deranlot, N. D. Mathur, S. Fusil, K. Bouzehouane, A. Barthelemy, *Science* **2010**, 327, 1106.

[21] J. Heron, M. Trassin, K. Ashraf, M. Gajek, Q. He, S. Yang, D. Nikonov, Y. Chu, S. Salahuddin, R. Ramesh, *Physical review letters* **2011**, 107, 217202.

[22] J. A. Mundy, C. M. Brooks, M. E. Holtz, J. A. Moyer, H. Das, A. F. Rébola, J. T. Heron, J. D. Clarkson, S. M. Disseler, Z. Liu, *Nature* **2016**, 537, 523.

[23] S. Zhang, Y. Zhao, P. Li, J. Yang, S. Rizwan, J. Zhang, J. Seidel, T. Qu, Y. Yang, Z. Luo, *Physical review letters* **2012**, 108, 137203.
[24] W. Eerenstein, M. Wiora, J. Prieto, J. Scott, N. Mathur, *Nature materials* **2007**, 6, 348.
[25] K. Cuschieri, D. H. Brewster, A. R. W. Williams, D. Millan, G. Murray, S. Nicoll, J. Imrie, A. Hardie, C. Graham, H. A. Cubie, *Phys Rev* **1946**, 70, 965.
[26] Q. Li, A. Tan, A. Scholl, A. T. Young, M. Yang, C. Hwang, A. T. N'Diaye, E. Arenholz, J. Li, Z. Q. Qiu, *Applied Physics Letters* **2017**, 110, 262405.
[27] R. P. Beardsley, S. Bowe, D. E. Parkes, C. Reardon, K. W. Edmonds, B. L. Gallagher, S. A. Cavill, A. W. Rushforth, *Scientific Reports* **2017**, 7, 7613.
[28] S. A. Cavill, D. E. Parkes, J. Miguel, S. S. Dhesi, K. W. Edmonds, R. P. Campion, A. W. Rushforth, *Applied Physics Letters* **2013**, 102, 032405.
[29] D. Parkes, R. Beardsley, S. Bowe, I. Isakov, P. Warburton, K. Edmonds, R. Campion, B. Gallagher, A. Rushforth, S. Cavill, *Applied Physics Letters* **2014**, 105, 062405.
[30] T. Ostler, R. Cuadrado, R. Chantrell, A. Rushforth, S. Cavill, *Physical review letters* **2015**, 115, 067202.
[31] C. Wang, X. Ke, J. Wang, R. Liang, Z. Luo, Y. Tian, D. Yi, Q. Zhang, J. Wang, X.-F. Han, *Nat Commun* **2016**, 7, 10636.
[32] R. Ullah, X. Ke, I. A. Malik, Z. Gu, C. Wang, M. Ahmad, Y. Yang, W. Zhang, X. An, X. Wang, J. Zhang, *ACS Appl Mater Interfaces* **2019**, 11, 7296.
[33] S. Yakata, M. Miyata, S. Nonoguchi, H. Wada, T. Kimura, *Applied Physics Letters* **2010**, 97, 1042.
[34] A. Yamaguchi, ., T. Ono, ., S. Nasu, ., K. Miyake, ., K. Mibu, ., T. Shinjo, . *Physical Review Letters* **2004**, 92, 077205.
[35] A. Thiaville, L. Belliard, D. Majer, E. Zeldov, J. Miltat, *Journal of applied physics* **1997**, 82, 3182.
[36] L. Q. Chen, *Journal of the American Ceramic Society* **2008**, 91, 1835.
[37] J. Fidler, T. Schrefl, *Journal of Physics D: Applied Physics* **2000**, 33, R135.
[38] N. Naoto, T. Yoshinori, *Nature Nanotechnology* **2013**, 8, 899.
[39] K. Shibata, J. Iwasaki, N. Kanazawa, S. Aizawa, T. Tanigaki, M. Shirai, T. Nakajima, M. Kubota, M. Kawasaki, H. Park, *Nature nanotechnology* **2015**, 10, 589.
[40] J. Wang, P. Wu, X. Ma, L. Chen, *Journal of Applied Physics* **2010**, 108, 114105.
[41] T. Zeng, H. Yan, H. Ning, J. Zeng, M. J. Reece, *Journal of the American Ceramic Society* **2009**, 92, 3108.
[42] H. Takeda, J. S. Han, M. Nishida, T. Shiosaki, T. Hoshina, T. Tsurumi, *Solid state communications* **2010**, 150, 836.
[43] L. Q. Chen, J. Shen, *Computer Physics Communications* **1998**, 108, 147.
[44] A. N. Bogdanov, *Low Temperature Physics* **1999**, 25, 151.
[45] H. B. Huang, X. Q. Ma, Z. H. Liu, C. P. Zhao, S. Q. Shi, L. Q. Chen, *Applied Physics Letters* **2013**, 102, 9353.
[46] J. M. Hu, T. Yang, J. Wang, H. Huang, J. Zhang, L. Q. Chen, C. W. Nan, *Nano Letters* **2015**, 15, 616.
[47] N. A. Pertsev, H. Kohlstedt, *Advanced Functional Materials* **2012**, 22, 4696.
[48] C. A. F. Vaz, J. A. C. Bland, G. Lauhoff, *Reports on Progress in Physics* **2008**, 71, 863.
[49] T. Nan, Z. Zhou, M. Liu, X. Yang, Y. Gao, B. A. Assaf, H. Lin, S. Velu, X. Wang, H. Luo, *Scientific Reports* **2014**, 4, 3688.

Figures

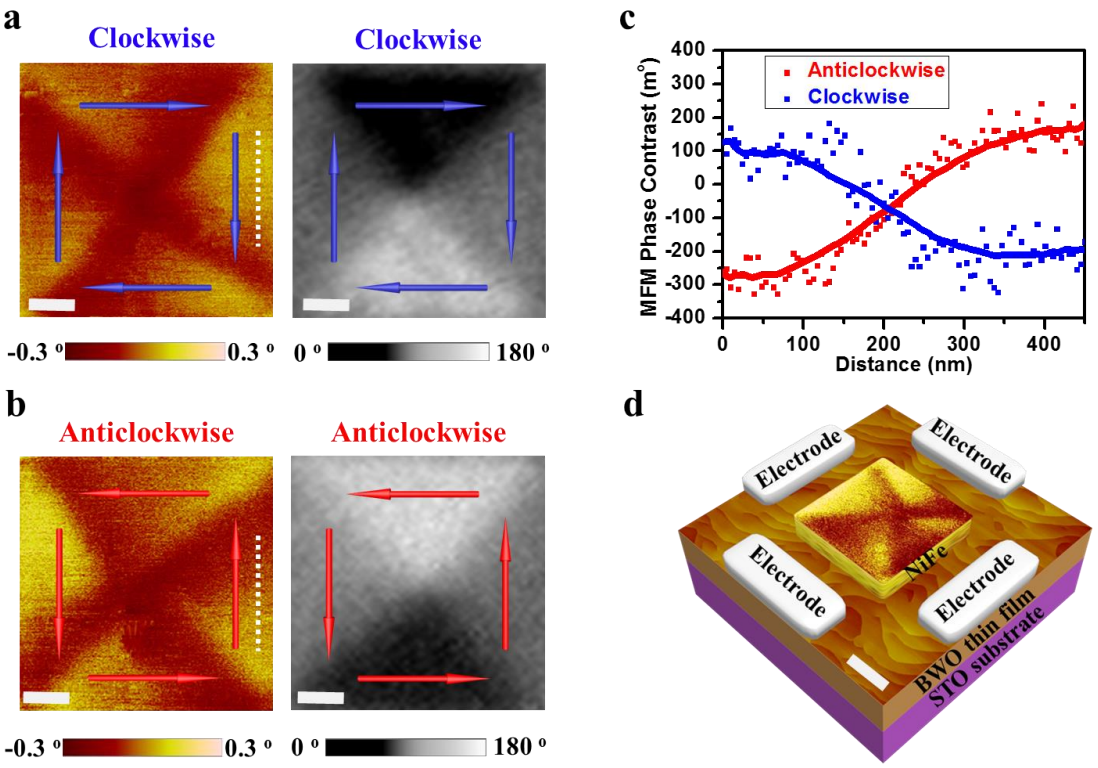

Figure 1. Characterization of magnetic vortex structure. a) A MFM image (left image) and the corresponding PFFM image (right image) show an as-grown vortex structure with clockwise circulation as indicated by the blue arrows. b) A MFM image (left image) and the corresponding PFFM image (right image) show an as-grown vortex structure with anticlockwise circulation as indicated by the red arrows. Scale bars, 250 nm (a-b). c) The MFM phase contrast measured by MFM indicates two as-grown vortex structures with clockwise and anticlockwise circulation respectively. The blue and red curves are extracted along the white dashed lines in (a) and (b) respectively. d) A geometry of the vortex structure (1×1 μm^2) with four planar electrodes fabricated on BWO thin film grown on STO substrate (a MFM image of the NiFe island is inserted). Scale bar, 250 nm.

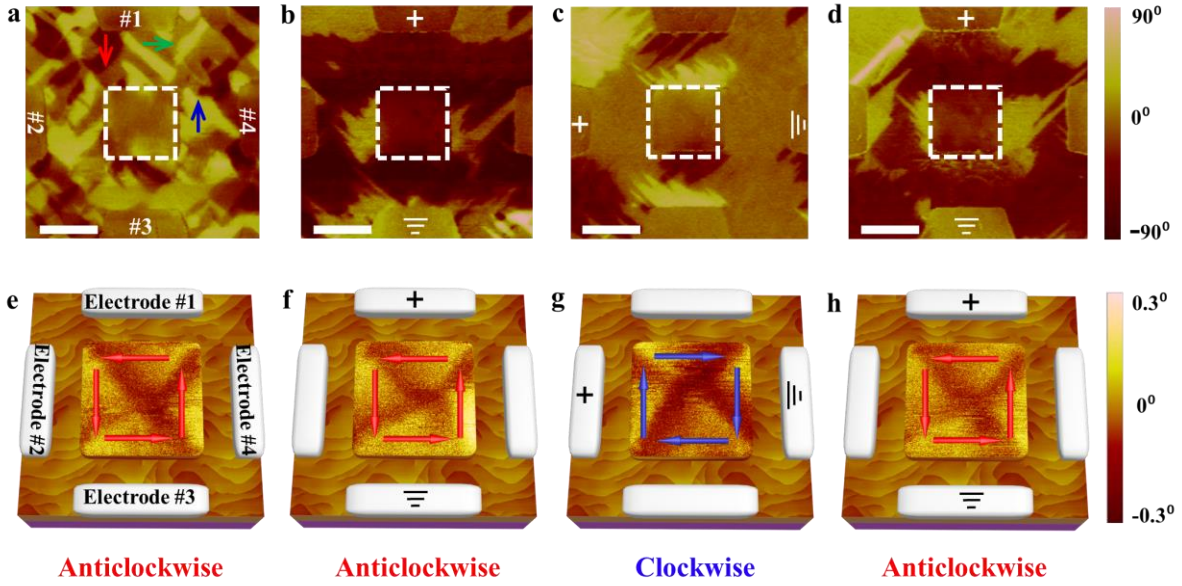

Figure 2. Vortex circulation reversal by electric field. a) A PFM image of the as-grown device with four electrodes marked as #1, #2, #3 and #4 respectively on top of BWO thin film. The polarization directions of the in-plane ferroelectric domains are indicated by the red, blue and green arrows respectively. b) The PFM image of the device after downward pulsed electric field of 500 $kVcm^{-1}$ applied using electrodes #1 and #3. c) The PFM image of the device after rightward pulsed electric field of 500 $kVcm^{-1}$ applied using electrodes #2 and #4. d) The PFM image of the device after downward pulsed electric field of 500 $kVcm^{-1}$ applied using electrodes #1 and #3. Scale bars, 1 μm (a-d). e) The MFM image of the as-grown vortex structure with anticlockwise circulation (indicated by red arrows) in the device corresponding to (a). f) The MFM image of the vortex structure with anticlockwise circulation (indicated by red arrows) after the application of the electric field corresponding to (b). g) The MFM image of the vortex structure with clockwise circulation (indicated by blue arrows) reversed after the application of the electric field corresponding to (c). h) The MFM image of the vortex structure with anticlockwise circulation (indicated by red arrows) reversed back after the application of the electric field corresponding to (d).

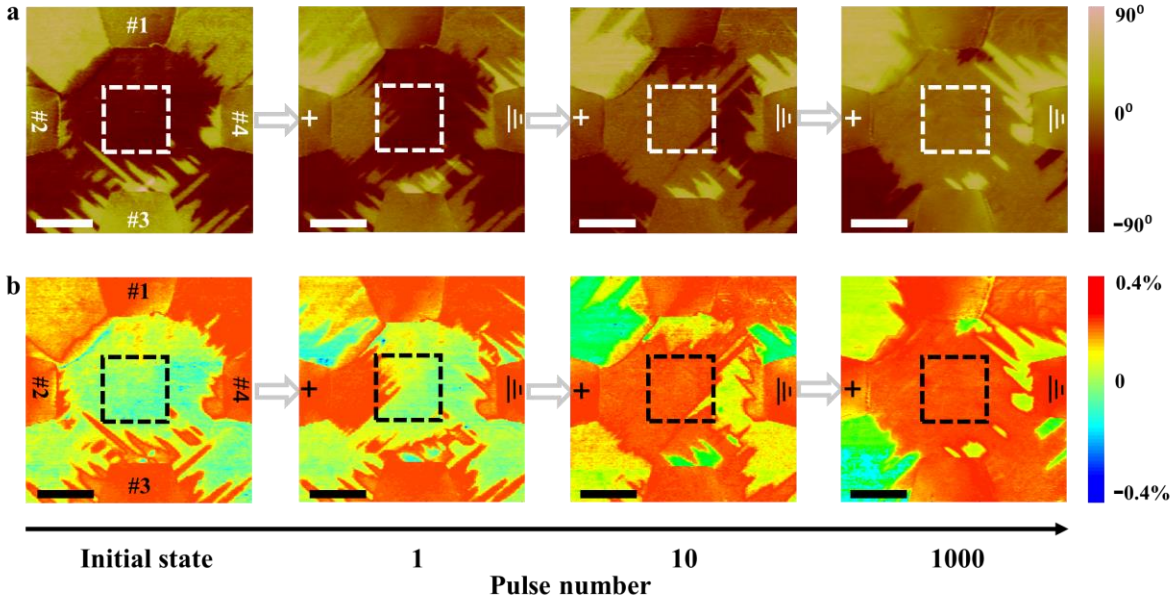

Figure 3. Varying strain under the electric field. a) PFM images of the device without NiFe island (indicated by the white dashed square) show a ferroelastic domain-wall motion as a function of pulsed electric field 500 $kVcm^{-1}$ using electrodes #2 and #4. b) The space-varying strain evolves as a function of pulsed electric field corresponding to (a). Scale bars, 1μm (a-b).

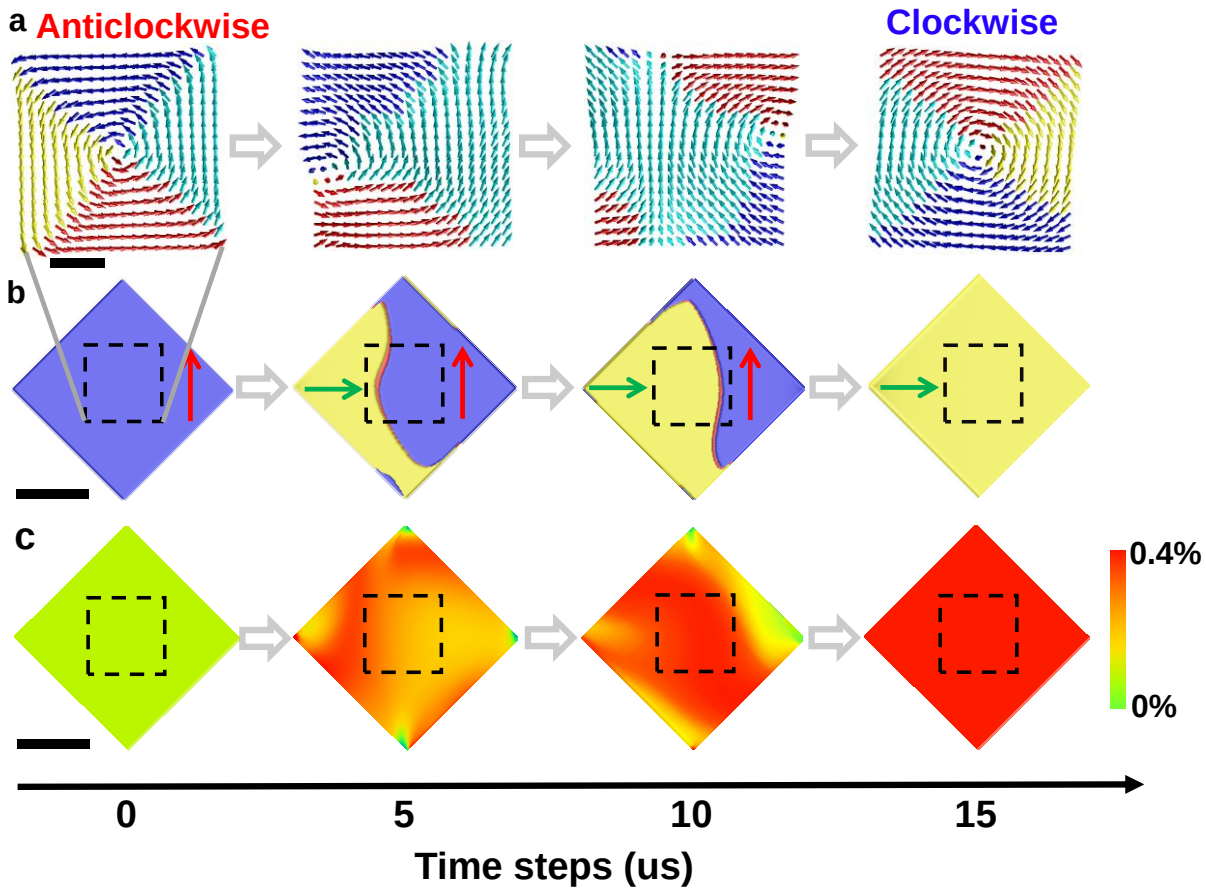

Figure 4. Dynamic mechanism of magnetic vortex reversal. a) A simulated reversal dynamic of vortex from initial anticlockwise circulation to clockwise circulation driven by a varying strain of 0.4% induced by the ferroelastic domain-wall motion along rightward direction, corresponding to the dark dashed square of vortex in (b-c). b) The process of the ferroelastic domain-wall motion along rightward corresponding to (a). c) The process of the varying strain evolution along rightward corresponding to (a). Scale bars are 250nm in (a) and 1μm in (b-c).